Fast Time-domain Imaging for One-stationary Bistatic Forward-looking SAR

Hongtu Xie, Daoxiang An, Xiaotao Huang, and Zhimin Zhou
College of Electronic Science and Engineering
National University of Defense Technology, Changsha, Hunan 410073, China

Abstract— In this paper, a fast time-domain imaging method called the fast backprojection algorithm (FBPA) is proposed for the one-stationary bistatic forward-looking synthetic aperture radar (OSBFSAR). First, the backprojection (BP) algorithm of the OSBFSAR is introduced. Then, the FBPA of the OSBFSAR based on the subaperture BP imaging is provided, and the sampling requirements of the polar subimage grid are derived from the bandwidth angle. Finally, the implementation of the proposed FBPA is discussed. Simulation results are shown to prove the validity of the proposed algorithm.

1. INTRODUCTION

One-stationary bistatic forward-looking synthetic aperture radar (OSBFSAR) [1] is a special bistatic SAR (BSAR) [2] system with a stationary radar fixed on the top of a high tower or mountain, working in the forward-looking mode [1]. It not only inherits the advantages of the BSAR, such as reducing vulnerability for military application and improving the detectability of stealth targets, but also carries out the high-resolution scene imaging in the forward direction [3]. However, its larger bistatic angle and synthetic aperture may induce the complicated range-azimuth coupling of echo data, which may increase the difficulty of the high-resolution imaging for the OSBFSAR [3].

Reconstructing the BSAR scene is performed by the BSAR imaging algorithms, divided into two classes: the frequency-domain algorithm and time-domain algorithm. The frequency-domain algorithms usually aim to minimize processing time, but it may lead to a number of limitations such as integration time, motion error, approximate processing, etc., which constrains its application. In contrast, the time-domain algorithms don't face to these limitations, but they require a high computational load. Time-domain backprojection algorithm (BPA) is considered as a linear transformation from the echo data into the SAR image, thus it can be applied directly to the OSBFSAR imaging [4]. To reduce the computational load, the fast implementation of the BPA has been used for the strip-map BSAR imaging, i.e., the fast backprojection algorithm (FBPA) and fast factorized backprojection algorithm (FFBPA) [5]. However, the FBPA has not been either mentioned or investigated for the OSBFSAR imaging in the earlier publications.

The aim of this paper is to present the FBPA to process the OSBFSAR echo data based on [5] Note that its availability is also used to the FFBPA since the processing principles of the FBPA and FFBPA are the same. Section 2 introduces the BPA for the OSBFSAR. Section 3 describes the proposed FBPA for the OSBFSAR imaging in detail. Section 4 proves its validity based on the simulation results. Section 5 gives the conclusion.

2. BPA FOR OBFSAR

Figure 1 shows the imaging geometry of the OSBFSAR. Moving radar moves along the straight line l_M parallel to the Y-axis direction at the speed V_M, with the position $\mathbf{r}_M(\eta) = (0, y_M(\eta), z_M)$ at the slow time η. The position of the stationary radar B is $\mathbf{r}_S = (x_S, 0, z_S)$. Assume that the scene is always illuminated by the stationary radar, and the moving radar operates in the forward-looking spotlight mode. P is an arbitrary scattering target in the scene, with the position $\mathbf{r}_P$. The ranges from the moving and stationary radars to the target P at η are $R_M(\eta, \mathbf{r}_P)$ and $R_S(\mathbf{r}_P)$, respectively. Thus, the traveling distance of a radar pulse radiated from the moving radar impinging on the target P, and then reflected to the stationary radar at η is

$$R(\eta, \mathbf{r}_P) = R_M(\eta, \mathbf{r}_P) + R_S(\mathbf{r}_P) = |\mathbf{r}_P - \mathbf{r}_M(\eta)| + |\mathbf{r}_P - \mathbf{r}_S|. \tag{1}$$

Provided that the transmitted signal is $p(\tau)$, after the demodulation and range compression, the received signal of the target P becomes

$$s_{rc}(\tau, \eta) = \sigma_p \cdot p_{rc}\left[B\left(\tau - R(\eta, \mathbf{r}_P)/c_0\right)\right]. \tag{2}$$

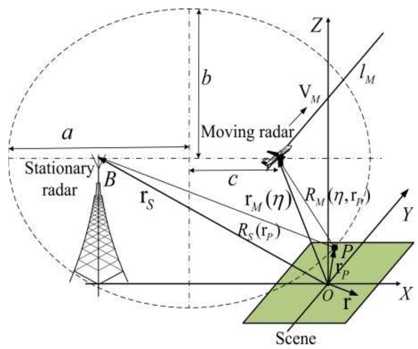

Figure 1: Imaging geometry of the OSBFSAR.

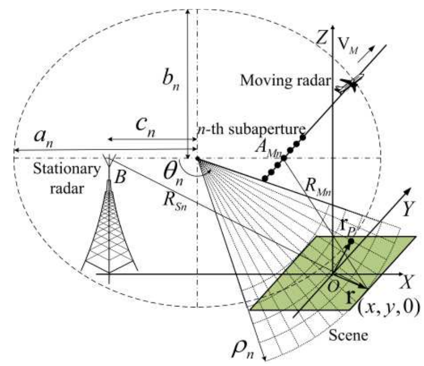

Figure 2: Subaperture imaging geometry.

where τ is the fast time, σ_P is the scattering coefficient of the target P, c_0 is the speed of light. $p_{rc}(\cdot)$ is the range compressed pulse, B is the transmitted signal bandwidth.

It is well known that the BPA can be applied for the OSBFSAR imaging without any modification The backprojection (BP) of the radar echo for the OSBFSAR case is performed over an ellipsoidal basis. a and b are the major and minor axes of the ellipse in Fig. 1, whose foci are the positions of the considered moving and stationary radars. The linear eccentricity is defined as $c = \sqrt{a^2 - b^2}$. $\mathbf{r} = (x, y, 0)$ is the position of an arbitrary sample in the scene, then the value of the SAR image at the sample $\mathbf{r}$ is

$$\begin{aligned} I(\mathbf{r}) &= \int_{\eta_c - T/2}^{\eta_c + T/2} s_{rc}\left(R(\eta, \mathbf{r})/c_0, \eta\right) \cdot \exp\left[j2\pi f R(\eta, \mathbf{r})/c_0\right] d\eta \\ &= \int_{\eta_c - T/2}^{\eta_c + T/2} \sigma_P \cdot p_{rc}\left[B\left((R(\eta, \mathbf{r}) - R(\eta, \mathbf{r}_P))/c_0\right)\right] \cdot \exp\left[j2\pi f R(\eta, \mathbf{r})/c_0\right] d\eta. \end{aligned} \tag{3}$$

η_c is the synthetic aperture center time, f is the radar frequency, T is the integration time.

3. FBPA FOR OSBFSAR

3.1. Subaperture BP Imaging

Figure 2 shows the n-th subaperture imaging geometry. A_{Mn} is the center of the n-th moving radar subaperture at the n-th subaperture center time η_n. The ranges from the moving and stationary radars to the sample $\mathbf{r}$ at η_n are R_{Mn} and R_{Sn}, respectively. a_n, b_n and c_n have the similar physical meanings as a, b and c in Fig. 1. The polar coordinates (ρ_n, θ_n) of the sample $\mathbf{r}$ are defined as following. First, the origin of a polar grid is the central point of the positions A_{Mn} and B. Second, ρ_n is the range between the origin of a polar grid and the sample $\mathbf{r}$, and θ_n is the angle from the major axis a_n to the range ρ_n. Thus, the polar coordinates (ρ_n, θ_n) are expressed as

$$\begin{cases} \rho_n = \sqrt{[x_S/2 - x]^2 + [y_M(\eta_n)/2 - y]^2 + [(z_S + z_M)/2]^2} \\ \theta_n = \arccos\left(\left(c_n^2 + \rho_n^2 - ((x_S - x)^2 + y^2 + z_S^2)\right)/2\rho_n c_n\right), \theta_n \in [0, \pi] \end{cases}. \tag{4}$$

Similarly, the polar coordinates (ρ_{np}, θ_{np}) of the target Pcan be also defined. T_n is the n-th subaperture integration time $R(\eta, \mathbf{r}_P) = R(\eta, \rho_{np}, \theta_{np})$ and $R(\eta, \mathbf{r}) = R(\eta, \rho_n, \theta_n)$ then the n-th polar subimage is

$$I_n(\rho_n, \theta_n) = \int_{\eta_n - T_n/2}^{\eta_n + T_n/2} \sigma_P \cdot p_{rc}\left[B\left((R(\eta, \rho_n, \theta_n) - R(\eta, \rho_{np}, \theta_{np}))/c_0\right)\right] \cdot \exp\left[j2\pi f R(\eta, \rho_n, \theta_n)/c_0\right] d\eta. \tag{5}$$

3.2. Sampling Requirements

To investigate the sampling requirements for the subimage polar grid, we need to calculate the bistatic range from the moving and stationary radars to the sample (ρ_n, θ_n). Fig. 3 shows the bistaitc range of the OSBFSAR. $A_{M\eta}$ is the moving radar position at η. $R_M(\eta, \rho_n, \theta_n)$ and $R_S(\rho_n, \theta_n)$ are the ranges from the positions $A_{M\eta}$ and B to the sample (ρ_n, θ_n). $\mu_{M\eta}$ is the range between positions

A_{Mn} and $A_{M\eta}$. $\vartheta_{M\eta}$ is the angle between the straight lines $\mu_{M\eta}$ and R_{Mn}, and $\psi_{M\eta}$ is the angle between the straight line $\mu_{M\eta}$ and the major axis a_n. φ_{Mn} is the angle between the straight line R_{Mn} and the major axis a_n. d_{Mn} is the length of the n-th moving radar subaperture, so $-d_{Mn}/2 \leq \mu_{M\eta} \leq d_{Mn}/2$. From Fig. 3, $R(\eta, \rho_n, \theta_n)$ in (5) can be computed and approximated as

$$\begin{aligned} R(\eta, \rho_n, \theta_n) &= \sqrt{R_{Mn}^2 + \mu_{M\eta}^2 - 2R_{Mn}\mu_{M\eta}\cos(\vartheta_{M\eta})} + R_S(\rho_n, \theta_n) \\ &\approx R_{Mn} - \mu_{M\eta}\cos(\vartheta_{M\eta}) + R_{Sn} \\ &\approx \sqrt{\rho_n^2 + c_n^2 + 2\rho_n c_n \cos(\theta_n)} + \sqrt{\rho_n^2 + c_n^2 - 2\rho_n c_n \cos(\theta_n)} \\ &\quad -\mu_{M\eta}\frac{c_n\cos(\psi_{M\eta}) + \rho_n\cos(\theta_n - \psi_{M\eta})}{\sqrt{\rho_n^2 + c_n^2 + 2\rho_n c_n\cos(\theta_n)}}. \end{aligned} \tag{6}$$

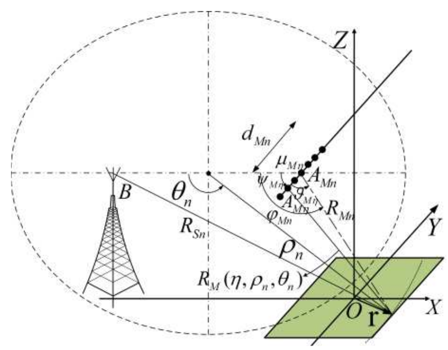

Figure 3: Bistatic range calculation for the OSBFSAR.

Two-dimensional Fourier transforms of $I_n(\rho_n, \theta_n)$ in (5) with respect to ρ_n and θ_n is given by

$$I_{FTn}(k_{\rho_n}, k_{\theta_n}) = \iint I_n(\rho_n, \theta_n) \exp\left[-j2\pi(k_{\rho_n}\rho_n + k_{\theta_n}\theta_n)\right] d\rho_n d\theta_n. \tag{7}$$

Fourier transform can be computed accurately by the principle of stationary phase. The phase condition is

$$\begin{cases} \partial\left(2\pi f R(\eta, \rho_n, \theta_n)/c_0 - 2\pi k_{\rho_n}\rho_n\right)/\partial\rho_n = 0 \\ \partial\left(2\pi f R(\eta, \rho_n, \theta_n)/c_0 - 2\pi k_{\theta_n}\theta_n\right)/\partial\theta_n = 0 \end{cases}. \tag{8}$$

Solving the above equations shows that $I_{FTn}(k_{\rho_n}, k_{\theta_n})$ is nonzero, when

$$\begin{cases} 2f_{\min}/\left(c_0\sqrt{1+\delta_n^2}\right) \leq k_{\rho_n} \leq 2f_{\max}/\left(c_0\sqrt{1+\delta_n^2}\right) \\ -f_{\max}d_{Mn}/\left(2c_0\sqrt{1+\delta_n^2}\right) \leq k_{\theta_n} \leq f_{\max}d_{Mn}/\left(2c_0\sqrt{1+\delta_n^2}\right) \end{cases}. \tag{9}$$

where $\delta_n$is defined as the ratio of c_n to ρ_n, (i.e., $\delta_n = c_n/\rho_n$). The bounds of k_{ρ_n} and k_{θ_n} can be translated directly into the sampling requirements of ρ_n and θ_n for the n-th polar subimage grid, then

$$\begin{cases} \Delta\rho_n \leq c_0\sqrt{1+\delta_n^2}/(2(f_{\max} - f_{\min})) \\ \Delta\theta_n \leq c_0\sqrt{1+\delta_n^2}/(f_{\max}d_{Mn}) \end{cases}. \tag{10}$$

It is seen that the range sampling space $\Delta\rho_n$ depends the signal bandwidth $f_{\max} - f_{\min}$ and factor δ_n, while angle sampling space $\Delta\theta_n$ depends the moving radar subaperture length d_{Mn} and the factors $f_{\max}$ and δ_n.

3.3. Implementation

The implementation of the proposed FBPA for the OSBFSAR is similar to the FBPA for the strip-map BSAR in [5], which can be also divided into two steps.

For the first step, the full aperture of the moving radar is split into several smaller subapertures, which requires the segmentation of the echo data in a same way. Then the polar subimage grids are defined and the regular BP for the considered subaperture is computed to generate the lowest-resolution polar subimages. For the second step, all the lower resolution polar subimages are interpolated into the Cartesian grid, and then the OSBFSAR image is reconstructed by a coherent combination of all the Cartesian subimages.

4. SIMULATION RESULTS

Simulation results are shown in this section to compare the performances of the proposed FBPA and BPA. The simulation parameters are shown in Table 1. The moving radar position at $\eta = 0$ is (0, 0, 500) m. Nine scattering targets labeled as $A \sim I$ are located in the scene (100 m $\times$ 100 m, range $\times$ azimuth), and the scene center position is (0 m, 0 m, 0 m), which are shown in Fig. 4(a). Both range and azimuth intervals of all scattering targets are 30 m, and the RCS of all scattering targets is assumed to be 1 m^2 for simplification.

Table 1: Simulation parameters of the OSBFSAR system.

Center frequency	Signal bandwidth	Sampling frequency	Pulse duration	PRF	Moving radar altitude (speed)	Stationary radar position
500 MHz	200 MHz	240 MHz	1 µs	100 Hz	200 m (45 m/s)	(−500, 0, 50) m

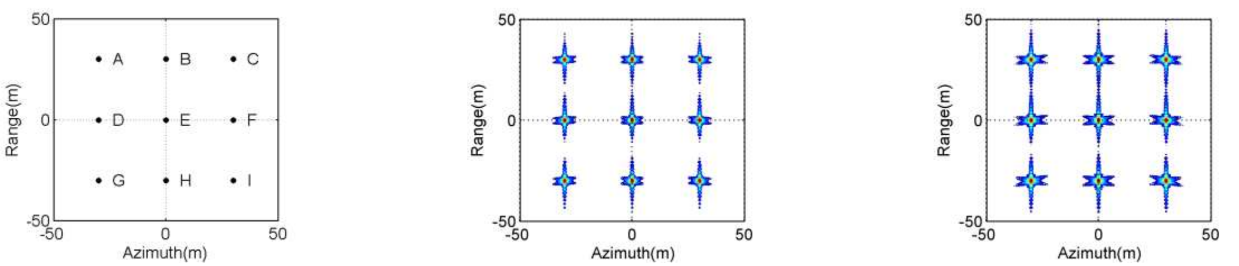

(a) (b) (c)

Figure 4: Imaging results obtained by the different algorithms. (a) Targets distribution; (b) BPA; (c) FBPA.

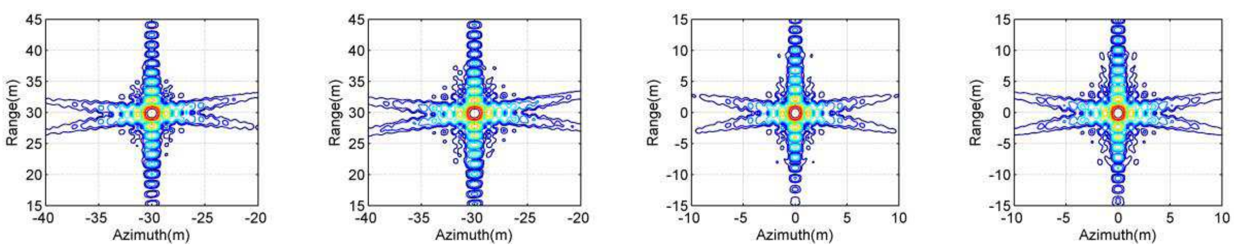

(a) (b) (c) (d)

Figure 5: Imaging results of targets A and E. (a) Imaging result of the target A extracted from Fig. 4(b); (b) Imaging result of the target A extracted from Fig. 4(c); (c) Imaging result of the target E extracted from Fig. 4(b); Imaging result of the target E extracted from Fig. 4(c).

Table 2: Measured parameters of the targets A and E.

Algorithms	Target A				Target E			
	Resolution (m)		PSLR (dB)		Resolution (m)		PSLR (dB)	
	Range	Azimuth	Range	Azimuth	Range	Azimuth	Range	Azimuth
BPA	1.282	0.814	−13.26	−13.30	1.358	0.732	−12.97	−13.40
FBPA	1.288	0.821	−13.27	−13.29	1.360	0.734	−12.95	−13.42

Figures 4(b) and 4(c) give the scene imaging results obtained by different algorithms. From Figs. 4(b) and 4(c), it is seen that all scattering targets are focused well. Fig. 5 give the contours of the imaging results of the targets A and E, which are extracted from Figs. 4(b) and 4(c). It is shown that the focusing performance of the targets A and E by the proposed FBPA is very similar to that by the BPA. The measured parameters of the targets A and E are calculated and listed in

Table 2. From Table 2, it is seen that the measured parameters of the targets A and E foucsed by the two algorithms are almost identical. The processing time of two algorithms is also measured, which is 107.2 s and 10.4 s for the BPA and proposed FBPA, respectively.

5. CONCLUSION

This paper presents a FBPA to focus the OSBFSAR echo data. This method reconstructs a SAR scene in the ground plane instead of the slant-range plane. First, the BPA of the OSBFSAR is introduced. Then, the FBPA of the OSBFSAR based on the subaperture BP imaging is provided, and then the sampling requirements of the polar subimage grid are derived from the bandwidth angle. Finally, the implementation of the proposed FBPA is discussed. This method can keep the accuracy and robust of the BPA but with a reduced computational load. The simulation results prove its validity.

ACKNOWLEDGMENT

This work was supported by the National Natural Science Foundation of China: Research on the key techniques of low frequency ultra wideband synthetic aperture radar interferometry (61201329) and Research Project of National University of Defense Technology (JC14-04-02).

REFERENCES

1. Espeter, T., I. Walterscheid, J. Klare, A. R. Brenner, and J. H. G. Ender, "Bistatic forward-looking SAR: Results of a spaceborne-airborne experiment," *IEEE Trans. Geosci. Remote Sens. Lett.*, Vol. 8, No. 4, 765–768, 2011.
2. Xie, H. T., D. X. An, X. T. Huang, and Z. M. Zhou, "Fast time-domain imaging in elliptical polar coordinate for general bistatic VHF/UHF ultra-wideband SAR with arbitrary motion," *IEEE J. Sel. Topics Appl. Earth Observ.*, Vol. 8, No. 2, 879–895, Feb. 2015.
3. Zhang, H. R., Y. Wang, and J. W. Li, "New application of parameter-adjusting polar format algorithm in spotlight forward-looking bistatic SAR processing," *Proc. APSAR*, 384–387, Tsukuba, Japan, 2013.
4. Xie, H. T., D. X. An, X. T. Huang, X. Y. Li, and Z. M. Zhou, "Fast factorised backprojection algorithm in elliptical polar coordinate for one-stationary bistatic very high frequency ultrahigh frequency ultra wideband synthetic aperture radar with arbitrary motion," *IET Radar Sonar Navig.*, Vol. 8, No. 8, 946–956, Oct. 2014.
5. Vu, V. T., T. K. Sjőgren, and M. I. Pettersson, "Fast time-domain algorithms for UWB bistatic SAR processing," *IEEE Trans. Aerosp. Electron. Syst.*, Vol. 49, No. 3, 1982–1994, 2013